

# Detecting and Mitigating Adversarial Attacks on Deep Learning-Based MRI Reconstruction Without Any Retraining

Mahdi Saberi<sup>\*†</sup>, Chi Zhang<sup>\*†§</sup>, Mehmet Akcakaya<sup>\*†</sup>

<sup>\*</sup>Department of Electrical and Computer Engineering, University of Minnesota

<sup>†</sup>Center for Magnetic Resonance Research, University of Minnesota

<sup>§</sup>Department of Radiology, Stanford University

{saber032, akcakaya}@umn.edu, zcglhf@stanford.edu

## Abstract

*Deep learning (DL) methods, especially those based on physics-driven DL, have become the state-of-the-art for reconstructing sub-sampled magnetic resonance imaging (MRI) data. However, studies have shown that these methods are susceptible to small adversarial input perturbations, or attacks, resulting in major distortions in the output images. Various strategies have been proposed to reduce the effects of these attacks, but they require retraining and may lower reconstruction quality for non-perturbed/clean inputs. In this work, we propose a novel approach for detecting and mitigating adversarial attacks on MRI reconstruction models without any retraining. Our detection strategy is based on the idea of cyclic measurement consistency. The output of the model is mapped to another set of MRI measurements for a different sub-sampling pattern, and this synthesized data is reconstructed with the same model. Intuitively, without an attack, the second reconstruction is expected to be consistent with the first, while with an attack, disruptions are present. Subsequently, this idea is extended to devise a novel objective function, which is minimized within a small ball around the attack input for mitigation. Experimental results show that our method substantially reduces the impact of adversarial perturbations across different datasets, attack types/strengths and PD-DL networks, and qualitatively and quantitatively outperforms conventional mitigation methods that involve retraining.*

## 1. Introduction

Magnetic resonance imaging (MRI) is an essential imaging modality in radiology and biomedical sciences, providing high-resolution images without ionizing radiation, and offering diverse soft-tissue contrast. However, its inherently long acquisition times may lead to patient discomfort and increased likelihood of motion artifacts, which degrade im-

age quality. Accelerated MRI techniques obtain a reduced number of measurements below Nyquist rate and reconstruct the image by incorporating supplementary information. Parallel imaging, which is the most clinically used approach, leverages the inherent redundancies in the data from receiver coils [13, 28, 33], while compressed sensing (CS) utilizes the compressibility of images through linear sparsifying transforms to achieve a regularized reconstruction [3, 14, 20, 29]. Recently, deep learning (DL) methods have emerged as the state-of-the-art for accelerated MRI, offering superior reconstruction quality compared to traditional techniques [4, 15, 23, 37]. In particular, physics-driven DL (PD-DL) reconstruction has become popular due to their improved generalizability and performance [2, 15, 17].

While PD-DL methods significantly outperform traditional MRI reconstruction techniques, these approaches have been shown to be vulnerable to small adversarial perturbations [12, 32], invisible to human observers, resulting in significant variations in the network’s outputs [5, 15, 44]. Various strategies to improve the robustness of PD-DL networks have been proposed to counter adversarial attacks in MRI reconstruction [7, 9, 19, 25, 34]. However, all these methods require retraining of the network, incurring a high computational cost, while also having a tendency to lead to additional artifacts for clean/non-attack inputs [41].

In this work, we propose a novel detection and mitigation strategy for adversarial attacks on DL-based MRI reconstruction, which does not require *any retraining*. Our approach utilizes the idea of cyclic measurement consistency [21, 39, 47, 49, 50] with synthesized undersampling patterns. The overarching idea for cyclic measurement consistency is to simulate new measurements from inference results with a new forward model that is from a similar distribution as the original forward model, which should be consistent with the original inference. This idea has been used to improve parallel imaging [50], then rediscovered in

the context of DL reconstruction training [21, 39, 49], and to introduce uncertainty guidance [47]. In our work, we use this idea in a completely novel direction to characterize and mitigate adversarial attacks. Succinctly, without an attack, reconstructions on synthesized measurements should be cycle-consistent, while with a small adversarial perturbation, there should be large discrepancies between reconstructions from actual versus synthesized measurements. For mitigation, we devise an objective function over the network input to ensure this idea of cyclic consistency, effectively mitigating the adversarial perturbations. Our contributions can be summarized as follows:

- We introduce a new method to detect adversarial perturbation in DL-based MRI reconstruction by comparing original and synthesized reconstructions, identifying attacks through a threshold on the change in the data fidelity error between these two reconstructions.
- We propose a novel mitigation strategy for adversarial attacks, which optimizes cyclic consistency over the input within a small ball, without requiring any retraining.
- We show that the mitigation strategy can be applied in a manner that is blind to the size of the perturbation or the algorithm that was used to generate the attack.
- Our method readily combines with existing robust training strategies to further improve reconstruction quality of DL-based MRI reconstruction under adversarial attacks.
- Our results demonstrate effectiveness across various datasets, PD-DL networks, attack types and strengths, and under-sampling patterns, outperforming existing methods qualitatively and quantitatively, without affecting the performance on non-perturbed images.

## 2. Background and Related Work

### 2.1. PD-DL Reconstruction for Accelerated MRI

In MRI, raw measurements are collected in the frequency domain, known as the k-space, using multiple receiver coils, where each coil is sensitive to different parts of the field-of-view. Accelerated MRI techniques acquire sub-sampled data, where the forward model is given as

$$\mathbf{y}_\Omega = \mathbf{E}_\Omega \mathbf{x} + \mathbf{n}, \quad (1)$$

where  $\mathbf{y}_\Omega$  is the measured data across all coils,  $\mathbf{E}_\Omega$  is the forward multi-coil encoding operator,  $\Omega$  is the undersampling pattern,  $\mathbf{n}$  is measurement noise, and  $\mathbf{x}$  is the image to be reconstructed [33]. The inverse problem for this acquisition model is formulated as

$$\arg \min_{\mathbf{x}} \|\mathbf{y}_\Omega - \mathbf{E}_\Omega \mathbf{x}\|_2^2 + \mathcal{R}(\mathbf{x}) \quad (2)$$

where the first quadratic term enforces data fidelity (DF) with the measurements, while the second term is a regularizer,  $\mathcal{R}(\cdot)$ . The objective in Eq. (2) is conventionally

solved using iterative algorithms [11] that alternate between DF and a model-based regularization term [11].

On the other hand, PD-DL commonly employs a technique called algorithm unrolling [31], which unfolds such an iterative reconstruction algorithm for a fixed number of steps. Here, the DF is implemented using conventional methods with a learnable parameter, while the proximal operator for the regularizer is implemented implicitly by a neural network [2, 15, 16, 37]. The unrolled network is trained end-to-end in a supervised manner using fully-sampled reference data [2, 15] using a loss of the form:

$$\arg \min_{\theta} \mathbb{E} \left[ \mathcal{L}(f(\mathbf{z}_\Omega, \mathbf{E}_\Omega; \theta), \mathbf{x}_{\text{ref}}) \right], \quad (3)$$

where  $\mathbf{z}_\Omega = \mathbf{E}_\Omega^H \mathbf{y}_\Omega$  is the zero-filled image that is input to the PD-DL network [16];  $f(\cdot, \cdot; \theta)$  is the output of the PD-DL network, parameterized by  $\theta$ , in image domain;  $\mathcal{L}(\cdot, \cdot)$  is a loss function;  $\mathbf{x}_{\text{ref}}$  is the reference image. Unsupervised training that only use undersampled data [4, 42] can be used, though this typically does not outperform supervised learning. In this work, we unroll the variable splitting with quadratic penalty algorithm [11], as in MoDL [2].

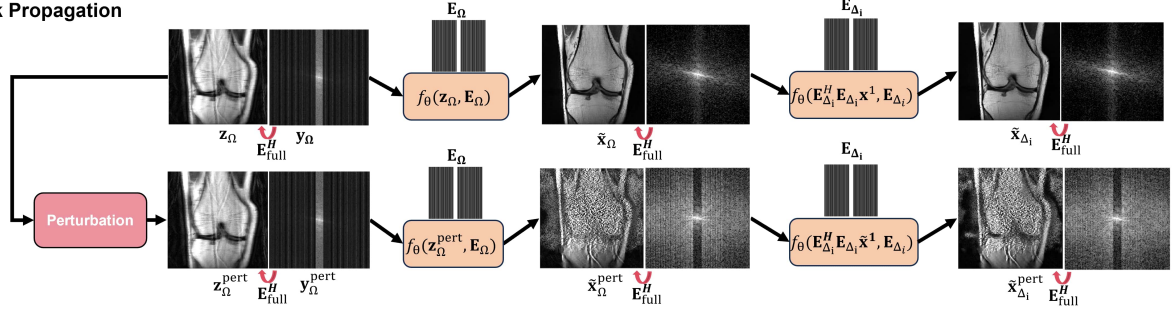
### 2.2. Adversarial Attacks in PD-DL MRI Reconstruction

Adversarial attacks create serious challenges for PD-DL MRI reconstruction, where small, visually imperceptible changes to input data can lead to large errors in the reconstructed image [5, 7, 48]. The main idea here is to find the worst-case degradation  $\mathbf{r}$  within a small  $\ell_p$  ball that will lead to the largest perturbation in the output of the network [5]:

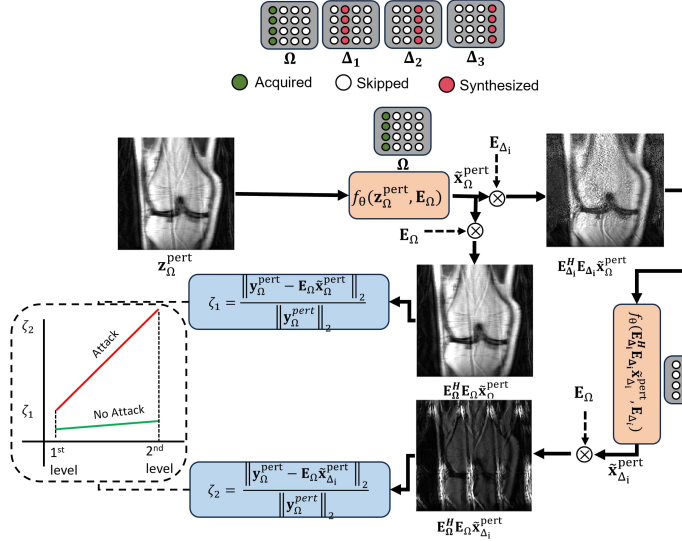
$$\arg \max_{\mathbf{r}: \|\mathbf{r}\|_p \leq \epsilon} \mathcal{L}(f(\mathbf{z}_\Omega + \mathbf{r}, \mathbf{E}_\Omega; \theta), f(\mathbf{z}_\Omega, \mathbf{E}_\Omega; \theta)). \quad (4)$$

We note that this attack calculation is unsupervised, which is the relevant scenario for MRI reconstruction [5, 19, 48], as the attacker cannot know the fully-sampled reference for a given undersampled dataset. In MRI reconstruction,  $\ell_\infty$  perturbations are commonly used in image domain [5, 19, 25, 48], while  $\ell_2$  perturbations are used in k-space [34] due to scaling differences between low and high-frequency in Fourier domain. In this work, we concentrate on the former, while examples for the latter are provided in SuppMat. Adversarial attacks are typically calculated using a gradient-based strategy [12, 30], where the input is perturbed in the direction of maximal change within the  $\ell_\infty$  ball. In this study, we use the iterative projected gradient descent (PGD) method [30], as it leads to more drastic perturbations than the single-step fast gradient sign method (FGSM) [12]. Further results with FGSM are included in SuppMat. Finally, we note that neural network based attacks have also been used [34], but these are mainly preferred for reduced computation time in training,

### a) Attack Propagation



### b) Attack Detection



### c) Attack Mitigation

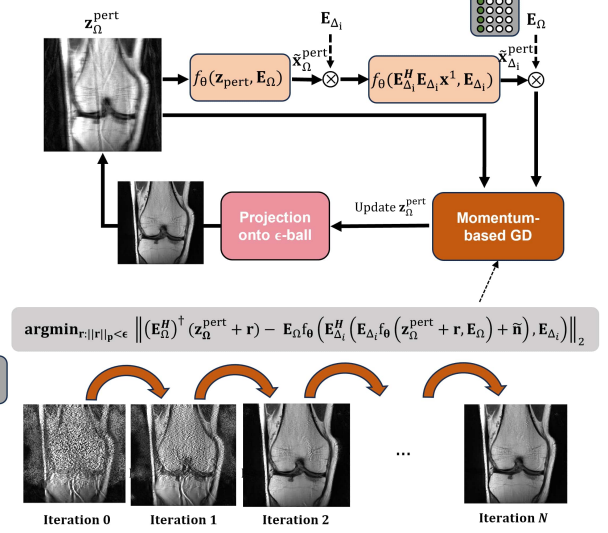


Figure 1. Proposed detection and mitigation strategy. a) If there is an adversarial attack, the k-space corresponding to the reconstructions of MRI data synthesized from previous DL model outputs will be disrupted. b) This idea is used to track the normalized  $\ell_2$  error on sampled k-space locations after reconstructions, and a large change in this error is indicative of an attack. c) A novel loss function is defined to find a “corrective” perturbation around the input that ensures cyclic measurement consistency.

and often fail to match the degradation caused by iterative optimization-based techniques [18].

### 2.3. Defense Against Adversarial Attacks in MRI Reconstruction

Incorporation of an adversarial term in the training objective is a common method for robust training, and has been proposed both in the image domain [19] or k-space [34]. The two common approaches either enforce perturbed outputs to the reference [19]:

$$\min_{\theta} \mathbb{E} \max_{\|\mathbf{r}\|_{\infty} \leq \epsilon} \mathcal{L}[f_{\theta}(\mathbf{z}_{\Omega} + \mathbf{r}, \mathbf{E}_{\Omega}; \theta), \mathbf{x}_{\text{ref}}] \quad (5)$$

or aim to balance normal and perturbed training [34]:

$$\min_{\theta} \max_{\|\mathbf{r}\|_{\infty} \leq \epsilon} \mathbb{E} \left[ \mathcal{L}[f_{\theta}(\mathbf{z}_{\Omega}, \mathbf{E}_{\Omega}; \theta), \mathbf{x}_{\text{ref}}] + \lambda \mathcal{L}[f_{\theta}(\mathbf{z}_{\Omega} + \mathbf{r}, \mathbf{E}_{\Omega}; \theta), \mathbf{x}_{\text{ref}}] \right], \quad (6)$$

where  $\lambda$  is a hyperparameter controlling the trade-off. While such training strategies improve robustness against adversarial attacks, it often comes at the cost of reduced performance on non-perturbed inputs [41]. Another recent method for robust PD-DL reconstruction proposes the idea of smooth unrolling (SMUG) [25]. SMUG [25] modifies denoised smoothing [36], introduces robustness to a regularizer part of the unrolled network. Each unrolled unit of SMUG performs:

$$\mathbf{x}_s^{i+1} = \arg \min_{\mathbf{x}} \|\mathbf{E}_{\Omega} \mathbf{x}_s^i - \mathbf{y}_{\Omega}\|_2^2 + \lambda \|\mathbf{x} - \mathbb{E}_{\eta}[\mathcal{D}_{\theta}(\mathbf{x}_s^i + \eta)]\|_2^2 \quad (7)$$

where  $\mathcal{D}_{\theta}$  represents the denoiser network with parameters  $\theta$ , and  $\eta \sim \mathcal{N}(\mathbf{0}, \sigma^2 \mathbf{I})$  is random Gaussian noise. During the training, SMUG [25] aims to incorporate  $N$  number of Monte Carlo sampling to smooth the denoiser outputs, averaging them before entering the next data fidelity block.

### 3. Proposed Method for Detecting & Mitigating Adversarial Attacks in PD-DL MRI

#### 3.1. Attack Propagation in Simulated k-space

The idea behind our detection and mitigation strategies stems from cyclic measurement consistency with synthesized undersampling patterns, which has been previously used to improve calibration/training of MRI reconstruction models [21, 39, 47, 49, 50]. For reconstruction purposes, a well-trained model should generalize to undersampling patterns with similar distributions as the acquisition one [23]. To this end, let  $\{\Delta_n\}$  be undersampling patterns drawn from a similar distribution as  $\Omega$ , including same acceleration rate, similar underlying distribution, *e.g.* variable density random, and same number of central lines. Further let

$$\tilde{\mathbf{x}}_\Omega = f(\mathbf{z}_\Omega, \mathbf{E}_\Omega; \theta) \quad (8)$$

be the reconstruction of the acquired data. We simulate new measurements  $\tilde{\mathbf{y}}_{\Delta_i}$  from  $\tilde{\mathbf{x}}$  using the encoding operator  $\mathbf{E}_{\Delta_n}$  with the same coil sensitivity profiles as  $\mathbf{E}_\Omega$ , and let  $\mathbf{z}_{\Delta_i} = \mathbf{E}_{\Delta_i}^H \tilde{\mathbf{y}}_{\Delta_i}$  be the corresponding zero-filled image. Then the subsequent reconstruction

$$\tilde{\mathbf{x}}_{\Delta_i} = f(\mathbf{z}_{\Delta_i}, \mathbf{E}_{\Delta_i}; \theta) \quad (9)$$

should be similar to  $\tilde{\mathbf{x}}_\Omega$ . In particular, we evaluate the similarity over the acquired k-space locations,  $\Omega$ , as we will discuss in Section 3.2. However, if there is an attack on the k-space, then this consistency with synthesized measurements are no longer expected to hold, as illustrated in Fig. 1a.

This can be understood in terms of what the PD-DL network does during reconstruction as it alternates between DF and regularization. The DF operation will ensure that the network is consistent with the input measurements,  $\mathbf{y}_\Omega$ , or equivalently the zero-filled image,  $\mathbf{z}_\Omega$ . If there is no adversarial attack, we expect the output of a well-trained PD-DL network to be consistent with these measurements, while also showing no sudden changes in k-space [23]. On the other hand, if there is an attack, the output will still be consistent with the measurements, as the attack is designed to be a small perturbation on  $\mathbf{y}_\Omega$  or  $\mathbf{z}_\Omega$ , and thus the small changes on these lines will be imperceptible. Instead, the attack will affect all the other k-space locations  $\Omega^C$ , the complement of the acquired index set, leading to major changes in these lines for the output of the PD-DL network, as depicted in Fig. 1a. Thus, when we resample a new set of indices  $\Delta_i$  that includes lines from  $\Omega^C$ , under attack the next level reconstruction  $\tilde{\mathbf{x}}_{\Delta_i}$  will no longer be consistent with the original k-space data  $\mathbf{y}_\Omega$ , as measured through  $\|\mathbf{y}_\Omega - \mathbf{E}_\Omega \tilde{\mathbf{x}}_{\Delta_i}\|_2$ . The distortion in the k-space will further propagate as we synthesize more levels of data and reconstruct these, if there is an adversarial attack.

#### 3.2. Attack Detection using Simulated k-space

The description of the attack propagation suggests a methodology for detecting these attacks. Noting that the process is best understood in terms of consistency with acquired data in k-space, we perform detection in k-space instead of attempting to understand the differences between subsequent reconstruction in image domain, which is not clearly characterized. In particular, we define two stages of k-space errors in terms of  $\mathbf{y}_\Omega$  for  $\tilde{\mathbf{x}}_\Omega$  and  $\tilde{\mathbf{x}}_{\Delta_i}$  as follows:

$$\zeta_1 = \frac{\|\mathbf{y}_\Omega - \mathbf{E}_\Omega \tilde{\mathbf{x}}_\Omega\|_2}{\|\mathbf{y}_\Omega\|_2}, \quad (10)$$

$$\zeta_2 = \frac{\|\mathbf{y}_\Omega - \mathbf{E}_\Omega \tilde{\mathbf{x}}_{\Delta_i}\|_2}{\|\mathbf{y}_\Omega\|_2}. \quad (11)$$

From the previous description  $\zeta_1$  is expected to be small with or without attack. However,  $\zeta_2$  is expected to be much larger under the attack, while it should be almost at the same level as  $\zeta_1$  without an attack. Thus, we check the difference between these two normalized errors,  $\zeta_2 - \zeta_1$ , and detect an attack if it is greater than a dataset-dependent threshold. The process is depicted in Fig. 1b, and summarized Algorithm 1.

---

#### Algorithm 1 Attack Detection

---

**Require:**  $\mathbf{z}_\Omega, \mathbf{E}_\Omega, \mathbf{E}_\Delta, f(\cdot, \cdot; \theta), \tau$   $\triangleright$  Input parameters  
**Ensure:** **True** or **False**, presence of attack  $\triangleright$  Output

- 1:  $\tilde{\mathbf{x}}_\Omega \leftarrow f(\mathbf{z}_\Omega, \mathbf{E}_\Omega; \theta)$
- 2:  $\mathbf{y}_{\Delta_i} \leftarrow \mathbf{E}_{\Delta_i} \tilde{\mathbf{x}}_\Omega + \tilde{\mathbf{n}}$
- 3:  $\tilde{\mathbf{x}}_{\Delta_i} \leftarrow f(\mathbf{E}_{\Delta_i}^H \mathbf{y}_{\Delta_i}, \mathbf{E}_{\Delta_i}; \theta)$
- 4:  $\zeta_1 = \frac{\|\mathbf{y}_\Omega - \mathbf{E}_\Omega \tilde{\mathbf{x}}_\Omega\|_2}{\|\mathbf{y}_\Omega\|_2}$
- 5:  $\zeta_2 = \frac{\|\mathbf{y}_\Omega - \mathbf{E}_\Omega \tilde{\mathbf{x}}_{\Delta_i}\|_2}{\|\mathbf{y}_\Omega\|_2}$
- 6: If  $\zeta_2 - \zeta_1 \geq \tau$  **True**, else **False**

---

#### 3.3. Attack Mitigation with Cyclic Consistency

Next, we describe our proposed mitigation strategy once an attack is detected. We note that adversarial attacks of Section 2.2 all aim to create a small perturbation within a ball around the original input. Here the size of the ball specifies the attack strength, the particular algorithm specifies how the attack is generated/propagated within the given ball, and the attack domain/norm specifies the type of  $\ell_p$  ball and whether it is in k-space or image domain.

Succinctly, our mitigation approach aims to reverse the attack generation process, by searching within a small ball around the perturbed input to find a clear input. The objective function for finding this clear input is based on the aforementioned idea of cyclic measurement consistency,



and is given as

$$\arg \min_{\mathbf{r}: \|\mathbf{r}\|_p \leq \epsilon} \mathbb{E}_{\Delta} \left[ \left\| (\mathbf{E}_{\Omega}^H)^{\dagger}(\mathbf{z}_{\Omega} + \mathbf{r}) - \mathbf{E}_{\Omega} f \left( \mathbf{E}_{\Delta}^H (\mathbf{E}_{\Delta} f(\mathbf{z}_{\Omega} + \mathbf{r}, \mathbf{E}_{\Omega}; \boldsymbol{\theta}) + \tilde{\mathbf{n}}), \mathbf{E}_{\Delta}; \boldsymbol{\theta} \right) \right\|_2 \right]. \quad (12)$$

Here  $\mathbf{r}$  is a small ‘‘corrective’’ perturbation and  $\mathbf{z}_{\Omega} + \mathbf{r}$  corresponds to the mitigated/corrected input. Hence the first term,  $(\mathbf{E}_{\Omega}^H)^{\dagger}(\mathbf{z}_{\Omega} + \mathbf{r})$  corresponds to the minimum  $\ell_2$  k-space solution that maps to this zero-filled image [48]. The second term is the corresponding k-space values at the acquired indices  $\Omega$  after two stages of cyclic reconstruction. Note as in Algorithm 1, a small noise term is added to the synthesized data to maintain similar signal-to-noise-ratio [22, 49]. The expectation is taken over undersampling patterns  $\Delta$  with a similar distribution to the original pattern  $\Omega$ .

The objective function is solved using a reverse PGD approach, which is detailed in Algorithm 2. Note the algorithm performs the expectation in Eq. (12) over  $K$  sampling pattern  $\{\Delta_k\}_{k=1}^K$ . Furthermore, to avoid getting stuck in local minima of this objective, we propose a momentum-based reverse PGD [30] approach for optimization, using an Adam-type updating rule, with the major change being the use of the  $\text{sgn}(\cdot)$  of the gradient for  $\ell_{\infty}$  constraints [30], as carried out in steps 11 and 12. The final step includes a projection on to the  $\epsilon$   $\ell_{\infty}$  ball.

---

#### Algorithm 2 Attack Mitigation

---

**Require:**  $\epsilon, \alpha, \mathbf{z}_{\Omega}^{\text{pert}}, \mathbf{E}_{\Omega}, \{\mathbf{E}_{\Delta_k}\}_{k=1}^K, f(\cdot, \cdot; \boldsymbol{\theta})$   $\triangleright$  Inputs

**Ensure:** Clean version of  $\mathbf{z}_{\Omega}^{\text{pert}}$   $\triangleright$  Mitigate attack on input

```

1:  $\tilde{\mathbf{z}}_{\Omega} = \mathbf{z}_{\Omega}^{\text{pert}}$ 
2: repeat
3:   Loss = 0
4:   for  $k = 1$  to  $K$  do
5:      $\tilde{\mathbf{y}}_{\Omega} = (\mathbf{E}_{\Omega}^H)^{\dagger} \tilde{\mathbf{z}}_{\Omega}$ 
6:      $\tilde{\tilde{\mathbf{y}}}_{\Omega} = \mathbf{E}_{\Omega} f(\mathbf{E}_{\Delta_k}^H (\mathbf{E}_{\Delta_k} f(\tilde{\mathbf{z}}_{\Omega}, \mathbf{E}_{\Omega}; \boldsymbol{\theta}) + \tilde{\mathbf{n}}), \mathbf{E}_{\Delta_k}; \boldsymbol{\theta})$ 
7:      $\text{loss}_k = \|\tilde{\mathbf{y}}_{\Omega} - \tilde{\tilde{\mathbf{y}}}_{\Omega}\|_2$   $\triangleright$  Eq. 12
8:     Loss = Loss +  $\text{loss}_k$ 
9:   end for
10:   $\mathbf{grad} = \frac{1}{K} \nabla_{\tilde{\mathbf{z}}_{\Omega}} \text{Loss}$ 
11:   $\mathbf{M}_{\mathbf{grad}} = \text{Adam}(\mathbf{grad})$   $\triangleright$  Adam Optimizer Grad.
12:   $\tilde{\mathbf{z}}_{\Omega} = \tilde{\mathbf{z}}_{\Omega} - \alpha \cdot \text{Sgn}(\mathbf{M}_{\mathbf{grad}})$ 
13:   $\tilde{\mathbf{z}}_{\Omega} = \text{Clip}_{\mathbf{z}_{\Omega}^{\text{pert}}, \epsilon}(\tilde{\mathbf{z}}_{\Omega})$   $\triangleright$  Projection to  $\epsilon$  ball
14: until Converge
```

---

Finally, note that this algorithm uses the strength of the attack. However, from a practical viewpoint, it may be beneficial to mitigate the attack without this information, which will not always be available to the end user. To this end, we propose a blind estimation procedure, where we estimate  $\epsilon$  and  $\alpha$  iteratively. First, we decrease  $\epsilon$  with a linear

scheduler for a fixed  $\alpha$ , starting from a large ball until convergence. Subsequently, we fix  $\epsilon$  and decrease  $\alpha$  similarly. The alternating process can be repeated, though in practice, one stage is sufficient. Finally, for blind mitigation, we always use  $\ell_{\infty}$  ball, even for  $\ell_2$  attacks in k-space discussed in SuppMat, as it contains the  $\ell_2$  ball of the same radius.

## 4. Experiments

### 4.1. Dataset Details

Our experiments were performed on publicly available fully-sampled multi-coil knee and brain MRI from fastMRI database [24], which have 15 and 20 receiver coils, respectively. For knee data, coronal proton density (Cor-PD) and coronal PD with fat suppression (Cor-PDFS) contrasts were used, while for brain data, axial FLAIR (Ax-FLAIR) was utilized. Retrospective equispaced undersampling was applied for acceleration  $R = 4$  to the fully-sampled data with 24 central auto-calibrated signal (ACS) lines.

### 4.2. Implementation Details

**Baseline Network.** The PD-DL network used in this study was a modified version of MoDL [2], unrolled for 10 steps, where a ResNet regularizer was used [17, 42, 43]. Further details about the architecture and training are provided in SuppMat. All the comparison methods were implemented using this MoDL network to ensure a fair comparison, except for the results on the applicability of our method to different PD-DL networks.

**Attack Generation Details.** PGD [30] was used to generate the attacks in an unsupervised manner, as detailed earlier for a realistic setup. Additional results with supervised attacks and FGSM are provided in SuppMat, and lead to the same conclusions. Complex images were employed to generate the attack and gradients, and MSE loss was used.

**Comparison Methods.** While we are unaware of any other works for detection, we compared our mitigation approach with existing robust training methods, including adversarial training [19, 34] and Smooth Unrolling (SMUG) [25]. Adversarial training was implemented using Eq. (5) [19],

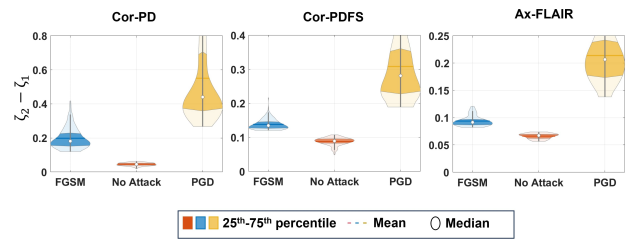


Figure 2. Attack detection for different datasets.  $\zeta_2 - \zeta_1$  for different attack types are clearly separated from the no attack case. The violin plots show the median and [25,75] percentile in darker colors for easier visualization.

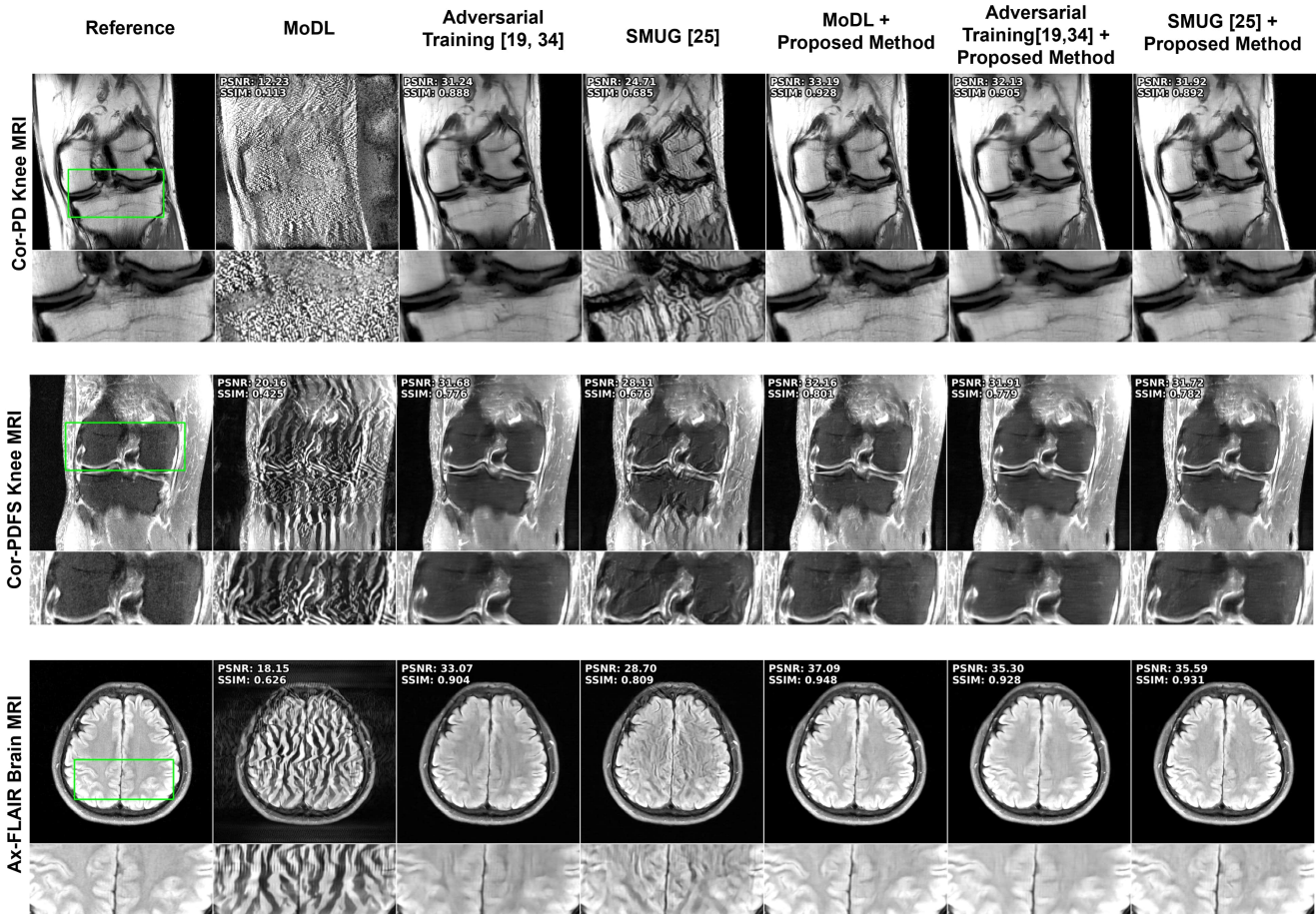


Figure 3. Representative reconstruction results for Cor-PD knee, Cor-PDFS knee, and Ax-FLAIR brain MRI Datasets at  $R = 4$ . The attack inputs lead to severe disruption in the baseline MoDL reconstruction. Adversarial training improves these, albeit suffering from blurriness. SMUG fails to eliminate the attack. The proposed strategy reduces the artifacts and maintains sharpness. Furthermore it can be combined with the other strategies for further gains (last two columns).

while results using Eq. (6) [34] is provided in SuppMat. Further implementation details for all methods are provided in SuppMat.

**Cyclic Consistency Details.** The synthesized masks  $\{\Delta_k\}$  were generated by shifting the equispaced undersampling patterns by one line while preserving the ACS lines [49]. In this setting, the number of synthesized masks is  $R - 1$ . For blind mitigation, the linear scheduler for  $\epsilon$  started from 0.04, and decreased by 0.01. For this estimated,  $\tilde{\epsilon}$ , the linear scheduler for  $\alpha$  started from  $\tilde{\epsilon}/2.5$  value and ended at  $\tilde{\epsilon}/5.5$ .

Table 1. Population metrics for SSIM/PSNR on all test slices

Dataset	Metric	SMUG	Adversarial Training (AT)	Proposed Method + MoDL / SMUG / AT
Cor-PD	PSNR	28.22	33.99	33.23 / 34.73 / <b>36.17</b>
	SSIM	0.79	0.92	0.92 / 0.92 / <b>0.94</b>
Cor-PDFS	PSNR	28.61	32.87	34.03 / 34.07 / <b>34.32</b>
	SSIM	0.62	0.79	<b>0.83 / 0.82 / 0.81</b>
Ax-FLAIR	PSNR	29.67	34.03	35.38 / 34.89 / <b>35.71</b>
	SSIM	0.84	0.91	<b>0.93 / 0.92 / 0.93</b>

### 4.3. Perturbation Detection Results

Figure 2 shows how  $\zeta_2 - \zeta_1$  changes for all datasets for both PGD and FGSM attacks on normalized zero-filled images for  $\epsilon = 0.01$ . It is clear that cases with an attack vs. non-perturbed inputs are separated by a dataset-dependent threshold. Note that given the sensitivity of PD-DL networks to SNR and acceleration rate changes, this dataset dependence is not surprising [22], and can be evaluated offline for a given trained model. Detection on other attack strengths are provided in SuppMat.

### 4.4. Attack Mitigation Results

This section summarizes all results for attack mitigation, and is sub-divided for each experiment, characterizing our mitigation strategy from different view points.

**Performance Across Datasets.** We first investigate our approach and other comparison methods across the three different brain and knee MRI datasets. Fig 3 shows rep-



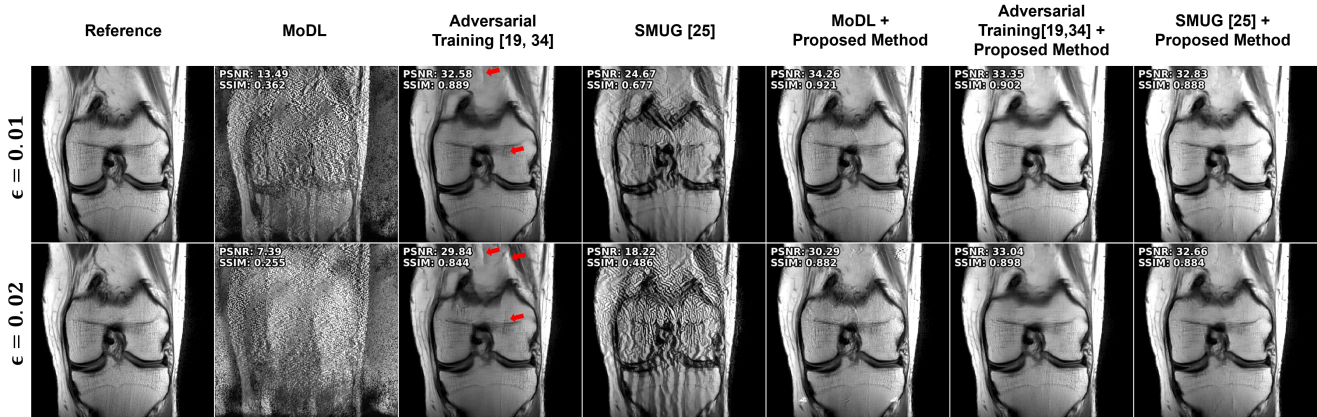


Figure 4. Performance across different attack strengths. Both Adversarial Training and the proposed method applied to MoDL work across different perturbation levels, with the proposed method leading to fewer visual artifacts in both.

representative results for  $R = 4$  for all methods. Baseline PD-DL, MoDL shows a high degree of artifacts under attack. SMUG is able to improve these but still suffers from substantial artifacts. Adversarial training resolves this artifacts, albeit with blurring. The proposed approach successfully mitigates the attacks *without any retraining*, while maintaining sharpness. We note our method can also be combined with SMUG and adversarial training to further improve their performance. Table 1 summarizes the quantitative metrics for all test slices in the datasets, which are consistent with the visual observations.

**Performance Across Error Strengths.** We next test the performance of the methods across different error strengths,  $\epsilon \in \{0.01, 0.02\}$ . Fig 4 shows the results for the robust methods trained with  $\epsilon = 0.01$  and the proposed method for both attack strengths. The results show SMUG fails to preserve the performance on both setups, while Adversarial Training and the proposed method have an acceptable mitigation on each attack strength. Adversarial Training

suffers from blurriness and visual artifacts, while the proposed method retains sharpness and details. Both methods show degraded PSNR/SSIM as a result of the stronger attack. Further quantitative results are provided in SuppMat.

**Performance Across Different PD-DL Networks.** Next, we hypothesize that our method is agnostic to the PD-DL architecture. To test this hypothesis, we perform our mitigation approach for different unrolled networks, including XPDNet [35], Recurrent Inference Machine [27], E2E-VarNet [38], and Recurrent-VarNet [46]. The implementation details are discussed in the SuppMat. Fig 5 depicts representative images for clear and perturbed inputs, and our proposed cyclic mitigation results. Overall, all networks show artifacts for perturbed inputs, while our proposed cyclic mitigation algorithm works well on all of them to reduce these artifacts. Further quantitative metrics for these networks are provided in SuppMat.

**Blind Mitigation Results.** These experiments show that in addition to not needing any retraining for mitigation, our approach does not require precise information about how the attack is generated. Fig. 6 shows how the reconstruction

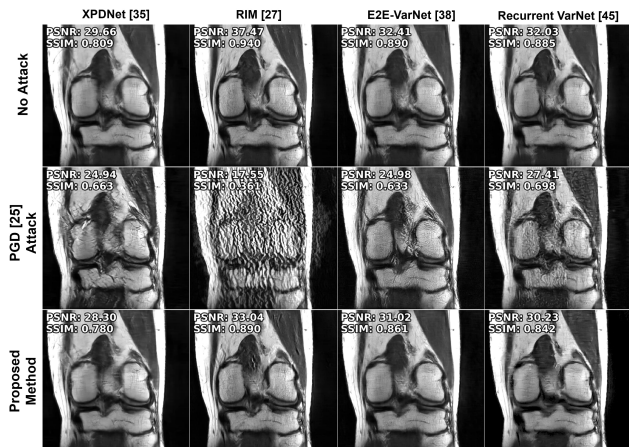


Figure 5. Proposed mitigation approach is readily applicable to various PD-DL networks for MRI reconstruction.

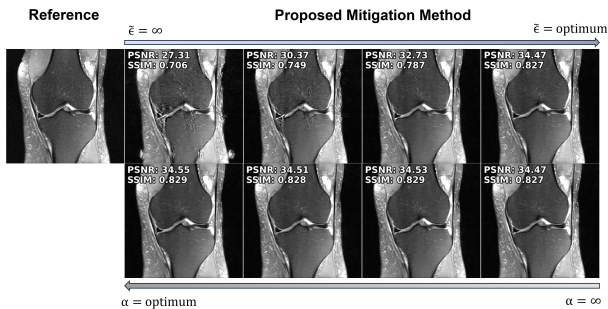


Figure 6. Blind mitigation process of finding the optimum  $(\epsilon, \alpha)$  parameters and corresponding results. Top row shows  $\epsilon$  optimization for a fixed  $\alpha$ , while the bottom row shows  $\alpha$  optimization for the optimum  $\epsilon$ .

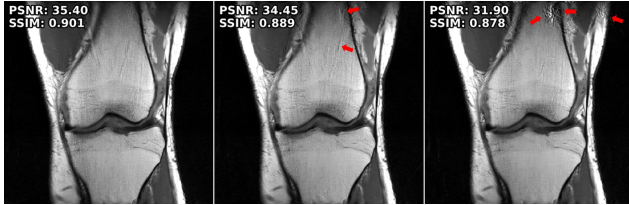


Figure 7. Ablation study on the number of stages for cyclic measurement consistency shows that 2 levels of reconstruction (left) is better than more levels (middle, right), as the latter has stronger reliance on synthesized k-space data.

improves as we use linear schedulers to find the optimum  $(\epsilon, \alpha)$  values. Top row shows the tuning of  $\epsilon$  while we keep the step size  $\alpha$  constant. After the cyclic loss in Eq. (12) stops decreasing, we fix this  $\bar{\epsilon}$  for the projection ball. The bottom row shows the effect of decreasing  $\alpha$  for this  $\bar{\epsilon}$  value, from right to left. Further results, including  $\ell_2$  k-space attacks and quantitative metrics are provided in SuppMat.

#### 4.5. Ablation Study

We perform an ablation study on how many level of reconstructions are needed for efficient detection and mitigation. For this task, one can naturally extend the definition of  $\zeta_1$  and  $\zeta_2$  to  $\zeta_j$ , which increases as the number of stages,  $j$  of reconstructions and data synthesis increase. We can reformulate this by updating the second term in the loss function in Eq. (12) to include more reconstruction stages. Here, we carry out the expectation over all possible permutations without repeating any patterns. As a result, the error propagated to the last stage becomes larger, as we rely more on synthesized data. In turn, this makes the optimization process harder, deteriorating the results, as shown in Fig. 7. In addition to these technical issues, adding more cyclic stages requires more computational resources which is not always practical. This suggests using 2-cyclic reconstruction stages is the best choice from both performance and computational perspectives.

### 5. Conclusions

In this study, we proposed a method to detect and mitigate small imperceptible adversarial input perturbations on DL-based MRI reconstructions, without requiring any re-training. We showed our method is robust across different datasets, attack strengths and unrolled networks. Additionally our method can be combined with existing robust training methods to further enhance their performance. Finally the proposed method can be performed in a blind manner without attack-specific information, such as attack strength or type for further practical applicability.

### References

- [1] Jonas Adler and Ozan Öktem. Learned primal-dual reconstruction. *IEEE Trans Med Imaging*, 37(6):1322–1332, 2018. 11
- [2] Hemant K Aggarwal, Merry P Mani, and Mathews Jacob. MoDL: Model-based deep learning architecture for inverse problems. *IEEE Trans Med Imaging*, 38(2):394–405, 2019. 1, 2, 5, 11, 13
- [3] Mehmet Akçakaya, Tamer A Basha, Beth Goddu, Lois A Goepfert, Kraig V Kissinger, Vahid Tarokh, Warren J Manning, and Reza Nezafat. Low-dimensional-structure self-learning and thresholding: regularization beyond compressed sensing for MRI reconstruction. *Magn Reson Med.*, 66(3):756–767, 2011. 1
- [4] Mehmet Akçakaya, Burhaneddin Yaman, Hyungjin Chung, and Jong Chul Ye. Unsupervised deep learning methods for biological image reconstruction and enhancement: An overview from a signal processing perspective. *IEEE Signal Process. Mag.*, 39(2):28–44, 2022. 1, 2
- [5] Vegard Antun, Francesco Renna, Clarice Poon, Ben Adcock, and Anders C Hansen. On instabilities of deep learning in image reconstruction and the potential costs of ai. *Proceedings of the National Academy of Sciences*, 117(48):30088–30095, 2020. 1, 2
- [6] Emre Cakır, Giambattista Parascandolo, Toni Heittola, Heikki Huttunen, and Tuomas Virtanen. Convolutional recurrent neural networks for polyphonic sound event detection. *IEEE/ACM Transactions on Audio, Speech, and Language Processing*, 25(6):1291–1303, 2017. 11
- [7] Francesco Calivá, Kaiyang Cheng, Rutwik Shah, and Valentina Pedoia. Adversarial robust training of deep learning MRI reconstruction models. *MELBA*, 2021. 1, 2
- [8] Antonin Chambolle and Thomas Pock. A first-order primal-dual algorithm for convex problems with applications to imaging. *J Math Imaging Vis*, 40:120–145, 2011. 11
- [9] Kaiyang Cheng, Francesco Calivá, Rutwik Shah, Misung Han, Sharmila Majumdar, and Valentina Pedoia. Addressing the false negative problem of deep learning MRI reconstruction models by adversarial attacks and robust training. In *Medical Imaging with Deep Learning*, pages 121–135. PMLR, 2020. 1
- [10] Kyunghyun Cho. Learning phrase representations using RNN encoder-decoder for statistical machine translation. *arXiv preprint arXiv:1406.1078*, 2014. 11
- [11] Jeffrey A Fessler. Optimization methods for magnetic resonance image reconstruction: Key models and optimization algorithms. *IEEE Sig Proc Mag*, 37(1):33–40, 2020. 2, 11
- [12] Ian J Goodfellow, Jonathon Shlens, and Christian Szegedy. Explaining and harnessing adversarial examples. *ICLR*, 2015. 1, 2, 12
- [13] Mark A Griswold, Peter M Jakob, Robin M Heidemann, Mathias Nittka, Volkmar Jellus, Jianmin Wang, Bernd Kiefer, and Axel Haase. Generalized auto-calibrating partially parallel acquisitions (grappa). *Magn Reson Med*, 47:1202–1210, 2002. 1
- [14] Justin P Haldar and Zhi-Pei Liang. Spatiotemporal imag-



- ing with partially separable functions: A matrix recovery approach. In *IEEE ISBI*, pages 716–719. IEEE, 2010. 1
- [15] Kerstin Hammernik, Teresa Klatzer, Erich Kobler, Michael P Recht, Daniel K Sodickson, Thomas Pock, and Florian Knoll. Learning a variational network for reconstruction of accelerated MRI data. *Magn Reson Med*, 79:3055–3071, 2018. 1, 2, 13
- [16] Kerstin Hammernik, Thomas Küstner, Burhaneddin Yaman, Zhengnan Huang, Daniel Rueckert, Florian Knoll, and Mehmet Akçakaya. Physics-driven deep learning for computational magnetic resonance imaging: Combining physics and machine learning for improved medical imaging. *IEEE Sig Proc Mag*, 40(1):98–114, 2023. 2
- [17] Seyed Amir Hossein Hosseini, Burhaneddin Yaman, Steen Moeller, Mingyi Hong, and Mehmet Akçakaya. Dense recurrent neural networks for accelerated MRI: History-cognizant unrolling of optimization algorithms. *IEEE J Sel Top Signal Process*, 14(6):1280–1291, 2020. 1, 5
- [18] Florian Jaeckle and M Pawan Kumar. Generating adversarial examples with graph neural networks. In *Uncertainty in Artificial Intelligence*, pages 1556–1564. PMLR, 2021. 3
- [19] Jinghan Jia, Mingyi Hong, Yimeng Zhang, Mehmet Akçakaya, and Sijia Liu. On the robustness of deep learning-based mri reconstruction to image transformations. *arXiv preprint arXiv:2211.04930*, 2022. 1, 2, 3, 5
- [20] Hong Jung, Kyunghyun Sung, Krishna S Nayak, Eung Yeop Kim, and Jong Chul Ye. k-t focuss: a general compressed sensing framework for high resolution dynamic mri. *Magn Reson Med*, 61(1):103–116, 2009. 1
- [21] Jeewon Kim, Wonil Lee, Beomgu Kang, Seohee So, and HyunWook Park. A noise robust image reconstruction deep neural network with cycle interpolation. In *Proc. ISMRM*, page 3717, 2023. 1, 2, 4
- [22] Florian Knoll, Kerstin Hammernik, Erich Kobler, Thomas Pock, Michael P Recht, and Daniel K Sodickson. Assessment of the generalization of learned image reconstruction and the potential for transfer learning. *Magn Reson Med*, 81(1):116–128, 2019. 5, 6
- [23] Florian Knoll, Kerstin Hammernik, Chi Zhang, Steen Moeller, Thomas Pock, Daniel K Sodickson, and Mehmet Akçakaya. Deep-learning methods for parallel magnetic resonance imaging reconstruction: A survey of the current approaches, trends, and issues. *IEEE Sig Proc Mag*, 37(1):128–140, 2020. 1, 4
- [24] Florian Knoll, Jure Zbontar, Anuroop Sriram, Matthew J Muckley, Mary Bruno, Aaron Defazio, Marc Parente, Krzysztof J Geras, Joe Katsnelson, Hersh Chandarana, et al. fastmri: A publicly available raw k-space and dicom dataset of knee images for accelerated mr image reconstruction using machine learning. *Radiology: Artificial Intelligence*, 2(1):e190007, 2020. 5
- [25] Shijun Liang, Van Hoang Minh Nguyen, Jinghan Jia, Ismail Alkhouri, Sijia Liu, and Saiprasad Ravishankar. Robust MRI reconstruction by smoothed unrolling (SMUG). *arXiv:2312.07784*, 2023. 1, 2, 3, 5
- [26] Pengju Liu, Hongzhi Zhang, Wei Lian, and Wangmeng Zuo. Multi-level wavelet convolutional neural networks. *IEEE Access*, 7:74973–74985, 2019. 11
- [27] Kai Lønning, Patrick Putzky, Jan-Jakob Sonke, Liesbeth Reneman, Matthan WA Caan, and Max Welling. Recurrent inference machines for reconstructing heterogeneous MRI data. *Medical Image Analysis*, 53:64–78, 2019. 7, 11
- [28] Michael Lustig and John M Pauly. SPIRiT: Iterative self-consistent parallel imaging reconstruction from arbitrary k-space. *Magn Reson Med*, 64(2):457–471, 2010. 1
- [29] Michael Lustig, David Donoho, and John M Pauly. Sparse MRI: The application of compressed sensing for rapid MR imaging. *Magn Reson Med*, 58(6):1182–1195, 2007. 1
- [30] Aleksander Mkadry, Aleksandar Makelov, Ludwig Schmidt, Dimitris Tsipras, and Adrian Vladu. Towards deep learning models resistant to adversarial attacks. *ICLR*, 2018. 2, 5, 11, 13
- [31] Vishal Monga, Yuelong Li, and Yonina C Eldar. Algorithm unrolling: Interpretable, efficient deep learning for signal and image processing. *IEEE Sig Proc Mag*, 38(2):18–44, 2021. 2
- [32] Seyed-Mohsen Moosavi-Dezfooli, Alhussein Fawzi, and Pascal Frossard. Deepfool: a simple and accurate method to fool deep neural networks. In *Proc CVPR*, pages 2574–2582, 2016. 1
- [33] Klaas P. Pruessmann, Markus Weiger, Markus B. Scheidegger, and Peter Boesiger. SENSE: Sensitivity encoding for fast MRI. *Magn Reson Med*, 42(5):952–962, 1999. 1, 2
- [34] Ankit Raj, Yoram Bresler, and Bo Li. Improving robustness of deep-learning-based image reconstruction. In *International Conference on Machine Learning*, pages 7932–7942. PMLR, 2020. 1, 2, 3, 5, 6, 12
- [35] Zaccharie Ramzi, Philippe Ciuciu, and Jean-Luc Starck. XPDNet for MRI reconstruction: An application to the 2020 fastMRI challenge. *arXiv:2010.07290*, 2020. 7, 11
- [36] Hadi Salman, Mingjie Sun, Greg Yang, Ashish Kapoor, and J Zico Kolter. Denoised smoothing: A provable defense for pretrained classifiers. *Advances in Neural Information Processing Systems*, 33:21945–21957, 2020. 3
- [37] Jo Schlemper, Jose Caballero, Joseph V Hajnal, Anthony N Price, and Daniel Rueckert. A Deep Cascade of Convolutional Neural Networks for Dynamic MR Image Reconstruction. *IEEE Trans Med Imaging*, 37(2):491–503, 2018. 1, 2
- [38] Anuroop Sriram, Jure Zbontar, Tullie Murrell, Aaron Defazio, C Lawrence Zitnick, Nafissa Yakubova, Florian Knoll, and Patricia Johnson. End-to-end variational networks for accelerated MRI reconstruction. In *MICCAI*, pages 64–73. Springer, 2020. 7, 11
- [39] Julián Tachella, Dongdong Chen, and Mike Davies. Unsupervised learning from incomplete measurements for inverse problems. *Proc NeurIPS*, pages 4983–4995, 2022. 1, 2, 4
- [40] Radu Timofte, Eirikur Agustsson, Luc Van Gool, Ming-Hsuan Yang, and Lei Zhang. Ntire 2017 challenge on single image super-resolution: Methods and results. In *Proc CVPR Workshops*, pages 114–125, 2017. 11
- [41] Dimitris Tsipras, Shibani Santurkar, Logan Engstrom, Alexander Turner, and Aleksander Madry. Robustness may be at odds with accuracy. *ICLR*. 1, 3
- [42] Burhaneddin Yaman, Seyed Amir Hossein Hosseini, Steen Moeller, Jutta Ellermann, Kâmil Uğurbil, and Mehmet

- Akçakaya. Self-supervised learning of physics-guided reconstruction neural networks without fully sampled reference data. *Magn Reson Med.*, 84(6):3172–3191, 2020. [2](#), [5](#), [11](#), [13](#)
- [43] Burhaneddin Yaman, Hongyi Gu, Seyed Amir Hossein Hosseini, Omer Burak Demirel, Steen Moeller, Jutta Ellermann, Kâmil Uğurbil, and Mehmet Akçakaya. Multi-mask self-supervised learning for physics-guided neural networks in highly accelerated magnetic resonance imaging. *NMR in Biomedicine*, 35(12), 2022. [5](#)
- [44] Guang Yang, Simiao Yu, Hao Dong, Greg Slabaugh, Pier Luigi Dragotti, Xujiang Ye, Fangde Liu, Simon Arridge, Jennifer Keegan, Yike Guo, et al. DAGAN: deep de-aliasing generative adversarial networks for fast compressed sensing MRI reconstruction. *IEEE Trans Med Imaging*, 37:1310–1321, 2017. [1](#)
- [45] George Yiasemis, Nikita Moriakov, Dimitrios Karkaloulos, Matthan Caan, and Jonas Teuwen. DIRECT: deep image REConstruction toolkit. *Journal of Open Source Software*, 7(73):4278, 2022. [11](#)
- [46] George Yiasemis, Jan-Jakob Sonke, Clarisa Sánchez, and Jonas Teuwen. Recurrent variational network: a deep learning inverse problem solver applied to the task of accelerated MRI reconstruction. In *Proc CVPR*, pages 732–741, 2022. [7](#), [11](#)
- [47] Chi Zhang and Mehmet Akçakaya. Uncertainty-guided physics-driven deep learning reconstruction via cyclic measurement consistency. In *2024 IEEE ICASSP*, pages 13441–13445, 2024. [1](#), [2](#), [4](#)
- [48] Chi Zhang, Jinghan Jia, Burhaneddin Yaman, Steen Moeller, Sijia Liu, Mingyi Hong, and Mehmet Akçakaya. Instabilities in conventional multi-coil MRI reconstruction with small adversarial perturbations. In *2021 55th Asilomar Conference on Signals, Systems, and Computers*, pages 895–899. IEEE, 2021. [2](#), [5](#)
- [49] Chi Zhang, Omer Burak Demirel, and Mehmet Akçakaya. Cycle-consistent self-supervised learning for improved highly-accelerated MRI reconstruction. In *2024 IEEE ISBI*, pages 1–5. IEEE, 2024. [1](#), [2](#), [4](#), [5](#), [6](#)
- [50] Tiejun Zhao and Xiaoping Hu. Iterative GRAPPA (iGRAPPA) for improved parallel imaging reconstruction. *Magn Reson Med*, 59(4):903–907, 2008. [1](#), [4](#)
- [51] Zongwei Zhou, Md Mahfuzur Rahman Siddiquee, Nima Tajbakhsh, and Jianming Liang. Unet++: A nested u-net architecture for medical image segmentation. In *Deep Learning in Medical Image Analysis and Multimodal Learning for Clinical Decision Support*, pages 3–11. Springer, 2018. [11](#)

## Supplementary Material

In these supplementary materials, we provide additional information on implementation details of different methods used in this study (Section A), and more examples and quantitative results summaries for attack variations discussed in the main text (Section B).

### A. Implementation Details

**MoDL** implementation is based on [2], unrolling variable splitting with quadratic penalty algorithm [11] for 10 steps. The proximal operator for the regularizer is implemented with a ResNet [42], and data fidelity term is implemented using conjugate gradient, itself unrolled for 10 iterations [2]. The ResNet comprises input and output convolutional layers, along with 15 residual blocks. Each residual block has a skip connection and two convolutional blocks with a rectified linear unit in between. At the end of each residual block, there is a constant scaling layer [40], and the weights are shared among different blocks [2].

**XPDNet** implementation is based on [45] and follows [35], which unrolls the primal dual hybrid gradient (PDHG) algorithm [8] for 10 steps. Each step contains k-space and image correction in sequence, where form the data fidelity and regularizer respectively. XPDNet applies the undersampling mask on the subtraction of the intermediate k-space with original measurements in k-space correction step. Image correction/regularizer is implemented using multi-scale wavelet CNN (MWCNN) [26] followed by a convolutional layer. Inspired by PDNet [1], it uses a modified version of PDHG to utilize a number of optimization parameters instead of just using the previous block’s output. 5 primal and 1 dual variables are used during the unrolling process, and the weights are not shared across the blocks.

**RIM** implementation based on [45] as described in [27] unrolls the objective for 16 time steps, where each utilizes a recurrent time step. Each time step takes the previous reconstruction, hidden states and the gradient of negative log-likelihood (as data fidelity term) and outputs the incremental step in image domain to take using a gated recurrent units (GRU) structure [10], where it utilizes depth 1 and 128 hidden channels. Parameters are shared across different recurrent blocks.

**E2E-VarNet** uses the publicly available implementation [38], and like variational networks, implements an unrolled network to solve the regularized least squares objective using gradient descent. The algorithm is unrolled for 12 steps. Each step combines data fidelity with a regularizer. Data fidelity term applies the under-sampling mask after subtraction of intermediate k-space from the measurements, while learned regularizer is implemented via U-Net [51], where it uses 4 number of pull layers and 18 number of output channels after first convolution layer. Weights are not

shared across blocks.

**Recurrent VarNet** uses the publicly available implementation [46] estimates a least squares variational problem by unrolling with gradient descent for 8 steps. Each iteration is a variational block, comprising data fidelity and regularizer terms. Data fidelity term calculates the difference between current level k-space and the measurements on under-sampling locations, where regularizer utilizes gated recurrent units (GRU) structure [6]. Each unroll block uses 4 of these GRUs with 128 number of hidden channels for regularizer. Parameters are not shared across different blocks [46].

As described in the main text, all methods were retrained on the respective datasets with supervised learning for maximal performance.

**Blind Mitigation Schedules.** For blind mitigation, our linear scheduler for  $\epsilon$  starts from 0.1 and decreases by 0.01 each step until the cyclic loss stabilizes. Then, step size  $\alpha$  starts from a large value of  $5\epsilon$  and is decreased by a step of  $\epsilon$  until the cyclic loss shows no further improvement. As mentioned in the main text, since the  $\ell_\infty$  ball contains the  $\ell_2$  ball of the same radius, and noting the unitary nature of the Fourier transform in regards to  $\ell_2$  attack strengths in k-space versus image domain, we always use the  $\ell_\infty$  ball for blind mitigation.

### B. Quantitative Results and Representative Examples

Due to space constraints, the figures and results in the main text focused on  $\ell_\infty$  attacks generated with unsupervised PGD [30], as mentioned in Section 4.2. This supplementary material section provides the corresponding results on related attack types mentioned in the main text.

#### B.1. Higher Attack Strengths

This subsection provides information referenced in Section 4.3 and 4.4.

**Attack Detection.** Fig. 8 shows violin plots of  $\zeta_2 - \zeta_1$  for  $\epsilon = 0.02$ , which is twice the strength used in Section 4.3 results. As expected, attacks are more easily distinguishable at higher attack strengths.

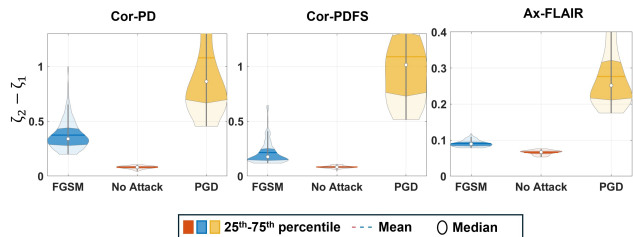


Figure 8. Attack detection for stronger attack,  $\epsilon = 0.02$ , shows  $\zeta_2 - \zeta_1$  is more easily distinguishable.



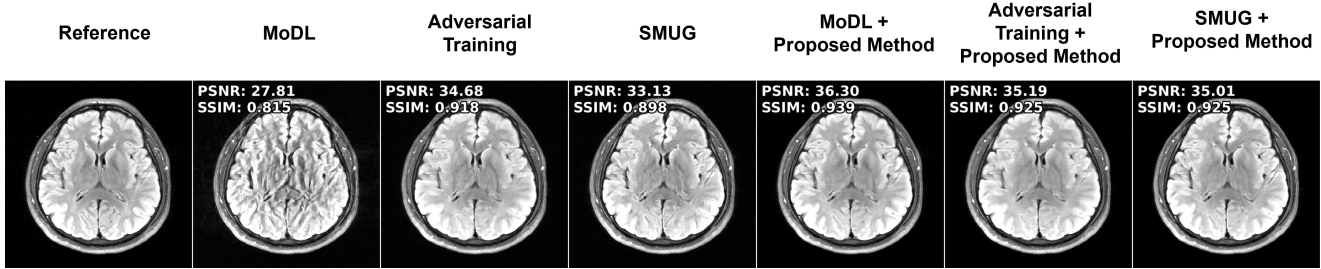


Figure 9. Performance of different methods under FGSM attack.

Table 2. Different attack strengths: Quantitative metrics on all test slices of Cor-PD

$\epsilon$	Metric	SMUG	Adversarial Training (AT)	Proposed Method + MoDL / SMUG / AT
0.01	PSNR	28.22	33.99	33.23/34.73/ <b>36.17</b>
	SSIM	0.79	0.92	0.92/0.92/ <b>0.94</b>
0.02	PSNR	21.86	30.91	28.67/33.97/ <b>35.65</b>
	SSIM	0.61	0.88	0.87/0.91/ <b>0.93</b>

**Quantitative Results on Attack Mitigation.** Table 2 summarizes the quantitative population metrics for different attack strengths,  $\epsilon$ , complementing the representative examples shown in Fig. 4 of Section 4.4. These quantitative results align with the visual observations.

## B.2. Quantitative Metrics for Different Networks

This subsection provides information referenced in Section 4.4. Table 3 shows that the quantitative metrics for the proposed attack mitigation strategy improve substantially compared to the attack for all unrolled networks, aligning with the observations in Fig. 5.

Table 3. Quantitative metrics for different unrolled networks

Network	Metric	With Attack	After Proposed Mitigation
XPDNet	PSNR	25.49	29.43
	SSIM	0.67	0.80
RIM	PSNR	19.63	34.81
	SSIM	0.39	0.90
E2E-VarNet	PSNR	24.24	29.52
	SSIM	0.59	0.84
Recurrent VarNet	PSNR	22.27	29.24
	SSIM	0.52	0.84

## B.3. Different Adversarial Training Methods

This subsection provides information referenced in Sections 2.3 and 4.2, specifically an alternative implementation of the adversarial training based on Eq. (6) with  $\lambda = 1$  to balance the perturbed and clean input, instead of Eq. (5) that was provided in the main text as a comparison. Results in Table 4 show that the version in the main text outperforms the alternative version provided here.

## B.4. Supervised Attacks

This subsection provides information referenced in Section 4.2. While the main text focused on unsupervised attacks

Table 4. Comparison of adversarial training approaches.

Method	Metric	With Attack
Adversarial Training (AT) with Eq. (5)	PSNR	33.99
	SSIM	0.92
AT with Eq. (6)	PSNR	33.61
	SSIM	0.91
AT with Eq. (5) + Proposed Method	PSNR	36.17
	SSIM	0.94
AT with Eq. (6) + Proposed Method	PSNR	36.91
	SSIM	0.94

due to practicality, here we provide additional experiments with supervised attacks, even though they are not realistic for MRI reconstruction systems. Table 5 shows that the proposed method is equally efficient in mitigating supervised attacks.

Table 5. Mitigation with Supervised vs. Unsupervised Attacks

Attack Method	Metric	Proposed Method
Unsupervised Attack	PSNR	32.44
	SSIM	<b>0.91</b>
Supervised Attack	PSNR	<b>32.55</b>
	SSIM	<b>0.91</b>

## B.5. FGSM Attack

This subsection provides information referenced in Sections 2.2 and 4.2. While the main text used PGD method for attack generation due to the more severe nature of the attacks, here we provide additional experiments with FGSM attacks [12]. Fig. 9 depicts representative reconstructions, showing that all methods perform better under FGSM compared to PGD attacks.

Table 6. FGSM attack: Quantitative metrics on all test slices of Ax-FLAIR

Metric	SMUG	Adversarial Training (AT)	Proposed Method + MoDL / SMUG / AT
PSNR	<b>36.24</b>	35.61	<b>36.24</b> / 35.13 / 36.06
SSIM	<b>0.93</b>	<b>0.93</b>	<b>0.93</b> / 0.92 / <b>0.93</b>

## B.6. $\ell_2$ Attacks in k-space

This subsection provides information referenced in Sections 2.2 and 4.4.  $\ell_2$  attacks have been used in k-space due to the large variation in intensities in the Fourier domain [34]. To complement the  $\ell_\infty$  attacks in image domain that was

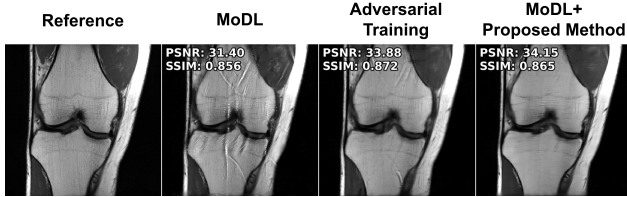


Figure 10. Representative reconstructions under  $\ell_2$  attack on measurements with  $\epsilon = 0.05 \cdot \|\mathbf{y}_\Omega\|_2$  using MoDL, adversarial training, and our proposed method.

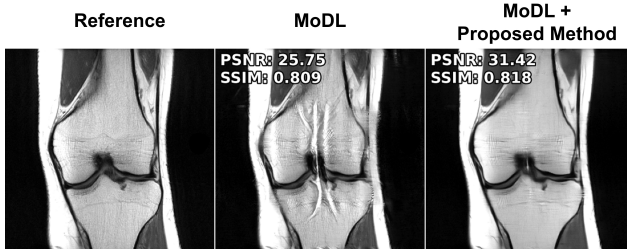


Figure 11. Representative reconstructions under  $\ell_2$  attack using MoDL and our proposed blind mitigation.

provided in the main text, here we provide results for  $\ell_2$  attacks in k-space, generated using PGD [30] for 5 iterations, with  $\epsilon = 0.05 \cdot \|\mathbf{y}_\Omega\|_2$  and  $\alpha = \frac{\epsilon}{5}$ . Fig. 10 depicts representative reconstructions with  $\ell_2$  attacks in k-space using baseline MoDL, adversarial training and our proposed mitigation. Table 8 shows comparison of adversarial training and the proposed method on Cor-PD datasets, highlighting the efficacy of our method in this setup as well.

Table 7. Attacks on non-uniform undersampling

Metric	MoDL	Adversarial Training (AT)	Proposed Method + MoDL / AT
PSNR	22.30	32.22	31.82/34.12
SSIM	0.62	0.89	0.87/0.92

### B.7. Further Blind Mitigation

This subsection provides information referenced in Section 4.4 on the effect of using blind mitigation for  $\ell_2$  attacks



Figure 12. Representative reconstructions for non-uniform undersampling reconstructions using MoDL, adversarial training, and our proposed method under adversarial attacks.

Table 8. Mitigation results for  $\ell_2$  attacks in k-space

Method	Metric	$\ell_2$ Attack
Adversarial Training	PSNR	33.37
	SSIM	0.88
Proposed Method + MoDL	PSNR	<b>34.21</b>
	SSIM	<b>0.89</b>

in k-space. Fig. 11 depicts example reconstructions with  $\ell_2$  attacks in k-space using baseline MoDL and our blind mitigation approach. Table 9 compares our blind mitigation approach to our mitigation strategy with known attack type and level, showing that blind mitigation performs on-par with the latter for both  $\ell_2$  attacks in k-space and  $\ell_\infty$  attacks in image domain.

Table 9. Blind mitigation for  $\ell_2$  (k-space,  $\epsilon = 0.05 \cdot \|\mathbf{y}_\Omega\|_2$ ) and  $\ell_\infty$  (image domain,  $\epsilon = 0.01$ ) attacks.

Attack Method	Metric	Proposed Method ( $\ell_\infty$ attack)	Proposed Method ( $\ell_2$ attack)
Knowing the Attack	PSNR	<b>33.23</b>	<b>34.21</b>
	SSIM	<b>0.92</b>	<b>0.89</b>
Blind Mitigation	PSNR	32.94	33.73
	SSIM	<b>0.92</b>	0.88

### B.8. Non-Uniform Undersampling Patterns

This subsection provides information referenced in Sections 1 and 4.4 on the use of different undersampling patterns. While the main text focused on uniform undersampling, which is considered to be a harder problem [15, 42], here we describe results with random undersampling, generated with a variable density Gaussian pattern [2]. All networks were retrained for such undersampling patterns. The attack generation and our mitigation algorithms were applied without any changes, as described in the main text.

Fig. 12 shows representative examples for different methods, highlighting that our method readily extends to non-uniform under-sampling patterns. Table 7 summarizes the quantitative metrics for this case, showing that the proposed mitigation improves upon MoDL or adversarial training alone.